

Fig. 2: Method overview of our teacher-student AD framework for 3D point cloud. In the training stage, the student network is trained on a specific normal sample category to learn multi-scale features to imitate the output of the corresponding teacher network. During the test stage, the degree of anomaly is calculated according to the similarity between the feature vectors of the teacher and the student.

categories. Such a beneficial property contributes to reducing the computational cost of retraining induced by the change of the normal category compared with the existing AD methods. Experiments conducted on a widely known point cloud dataset demonstrate superior anomaly detection performance with only few normal samples for training.

In summary, our paper includes the following main contributions:

- We first adopt a teacher-student structure embedded with PointNet for anomaly detection with respect to 3D point cloud, which facilitates training with few normal samples.
- We design a multi-scale loss to seamlessly merge the pooled features at different layers during network optimization to boost the detection performance.
- We conduct extensive experiments and ablation studies to qualitatively and quantitatively demonstrate the state-of-the-art AD accuracy of our method against prior methods.

II. RELATED WORK

In this section, we first review some anomaly detection methods for 3D point cloud. Then, we introduce the applications of teacher-student structure-based anomaly detection. We finally give a comprehensive introduction to anomaly detection techniques involving few sample training strategy.

A. Anomaly Detection for 3D Point Clouds

It is worth mentioning that AD for 3D point cloud has been explored very little to date. To the best of our knowledge, [23] and [6] are the only two explorations of this field. [6] first adopted the teacher-student network to compute the regression error as the anomaly score for 3D anomaly detection, and the teacher network is pretrained by reconstructing local receptive fields. This work focuses on point-wise anomaly detection, and the feature extracted from the point cloud with color

information is dense and represented in the form of 3D descriptors. As for the dataset they used (MVTec 3D-AD dataset [5]), since the object is located within a limited region and the cameras are well calibrated, the effect induced by the geometric transformation of the object can be largely disregarded. On the other hand, at this point, our problem setting is more challenging because the extracted features should be invariant to rotations, translations, and scale change, which is the main reason for using PointNet as the feature extractor in this paper. [23] proposed a VAE-based AD framework for 3D point cloud. This method handles AD for general objects represented by 3D points. However, reconstruction often incurs huge computational expense. Additionally, achieving a quality reconstructing capability generally involves a large number of training samples, which makes it less applicable in the real world. Contrarily, since we exploit the teacher-student distillation scheme, our method shows less reliance on sample number compared with reconstruction-based methods.

B. Anomaly Detection with Teacher-Student Networks

Teacher-student-based methods [4], [33], [28], [19], [10], [30] have been extensively studied in the field of AD, particularly focused on 2D images. [4] proposed a teacher-student framework for unsupervised anomaly detection with discriminative latent embeddings to efficiently construct a descriptive teacher network. In addition, a dedicated network design can exploit more information from the rich features. [33], [28] leveraged both coarse and fine levels of features by incorporating a multi-scale training scheme into the teacher-student framework. Despite the remarkable performance, these methods are limited to handling AD for 2D images only.

Later efforts then extended the teacher-student framework to explore wider applications for other forms of data. [19] proposed an adaptive framework to understand scene dynamics from audio-visual data in a hybrid fusion manner. [10] proposed

a reserved distillation method by using a one-class bottleneck embedding (OCBE) module to boost the discrimination capability. Overall, a crucial problem for these methods is that a large number of normal samples are required for training, yet it is not always feasible to acquire sufficient training data. Moreover, since they involve retraining procedures to tackle another normal category assumption, retraining on all the categories can result in highly expensive computational consumption.

C. Few Samples-based Anomaly Detection

To alleviate the reliance on large training samples, recent works have shifted to exploring few samples-based AD techniques. Because of the inherent difficulty that a quality generalization ability generally involves more than thousands of samples [22], [3], [36], AD with few samples has still been treated very sparsely. Here, we investigated two approaches related to few-samples training in a broader context: the few-shot approach and the data augmentation approach.

As for the few-shot based methods, in [29], a multilevel VAE is proposed to separate domain-level features from sample-level features for domain generalization with few samples. In [24], a novel prior-driven model is created to achieve an end-to-end differentiable learning of fine-grained anomaly score by utilizing a small number of labeled anomalies with a Gaussian prior. To address the over-fitting problem when dealing with sparsely labeled data, the authors of [44] designed a Siamese Convolutional Neural Network (CNN)-based model with a relative-feature representation scheme. A hierarchical generative model was utilized in [31] to capture the multi-scale patch distribution of few training images. In [41], a model-agnostic meta-learning model (MAML) is proposed, which can quickly adapt to unseen tasks with an inner loop and an outer loop inside to detect anomalies with few samples.

There are also works to artificially increase the amount of data for solving the few samples problem (i.e., data augmentation). In [43], they randomly masked out the square regions of an input image, named ‘‘Cutout’’, to realize automated surface inspection. To overcome the tedious laboring efforts in manual annotation, several generative model-based data augmentation techniques [13], [40] have been proposed. [13] employed a Generative Adversarial Network (GAN)-based augmentation scheme to synthesize additional images for surface defect detection. [40] proposed using the Conditional Variational Auto-Encoder (CVAE) to generate diverse defect images by sampling from the learned latent space. [32] proposed a two-stage deep learning scheme for defect detection with only few true defect samples by using CycleGAN [45] to synthesize and annotate defect pixels in an image automatically. [14] first learned to extract the attention maps for each image, based on which the dataset is augmented in a weakly supervised manner. In general, these methods only focus on addressing data augmentation for 2D images.

Comparing with these potential solutions, our model benefits from the use of a teacher-student framework and multi-scale feature extraction in the 3D point cloud scenario. The reasons lie in that: (i) it allows the student to learn how to specifically

extract necessary features from a powerful pretrained teacher network according to the concept of knowledge distillation, which can combat the tendency of the precision loss issue induced by over-valuing generalization performance in few-shot-based models; (ii) by incorporating multi-scale modules into our framework, the student network can learn both coarse and fine features from few training samples, which is more straightforward and unified since it frees synthetically generating scaled or transformed data for training.

III. METHOD

Fig. 2 illustrates the overview of our method for detecting anomaly with respect to point cloud. Our network is constituted of a teacher-student network pair. The teacher network is first pretrained to characterize the deep features of point cloud for all categories using the feature extraction block adopted from PointNet [26]. The student network, which is structured identically to the teacher network, then learns to effectively match the features for a required category of point cloud with the teacher counterparts. Furthermore, we introduce several pooling modules at different scales between the teacher and the student networks, and design a multi-scale loss calculated with all the pooling outputs to fully utilize the features to guide the student network. During inference, we compute the cosine similarity-based metric between the outputs of the teacher and student networks as the anomaly score to evaluate the degree of anomaly. Specifically, given the assumed normal point cloud samples of a certain category, the student network learns to predict the corresponding output feature embedded by the pretrained teacher network during training process (blue arrows in Fig. 2). During the test process, the anomaly score is calculated based on the similarity between the feature vectors outputted by student and teacher (orange arrows in Fig. 2). Lower similarity indicates a higher degree of anomaly. In the rest of this section, we first detail our teacher-student framework with PointNet. We then specify our multi-scale optimization strategy. Eventually, we elaborate on the inference procedure of anomaly detection.

A. Teacher-Student Structured PointNet for 3D Anomaly Detection

Teacher network. We first detail the training policy for the teacher network. Formally, we define a set of point cloud data as $\mathcal{M}^c = \{\mathbf{M}_1^c, \dots, \mathbf{M}_m^c, \dots, \mathbf{M}_{N_c}^c\}$ for the c -th object category with N_c point clouds, where each point cloud $\mathbf{M}_m^c = \{\mathbf{p}_1, \dots, \mathbf{p}_w, \dots, \mathbf{p}_W\}$ contains W 3D points represented by their coordinates (x, y, z) (i.e., $\mathbf{p}_w \in \mathbb{R}^3$). The teacher network is leveraged as a powerful feature extractor to obtain quality deep features for point cloud to facilitate distillation. To realize this, we design our teacher network based on the architecture of the PointNet segmentation network [26]. As for the pretraining of the teacher network, the input raw points \mathcal{M}^c fed to the teacher network is first transformed for alignment and then goes through a Multilayer Perceptron (MLP) encoding module to be encoded into the feature space. The features are again aligned, and then lifted to higher dimensions. Eventually, the features at different layers are concatenated as a mixture into the final segmentation module. As such, by optimizing the

segmentation loss (i.e., cross-entropy), the features in each layer can be gradually refined to capture meaningful features with different scales.

We pretrain the teacher network on the whole point cloud dataset $\mathcal{M} = \{\mathcal{M}^c | c = 1, \dots, C\}$ to guarantee a complete learning of features for all types of objects. Since the eventual aim of the teacher lies solely in feature extraction, during the training of the teacher-student network, we remove the segmentation module to form the final teacher network. After acquiring a teacher network pretrained on the segmentation task, we next need to determine the corresponding student network to fulfill the task of AD for point cloud.

Student network. The target of the student network is to learn to model a specific category (i.e., selected normal category) of point cloud under the guidance of the pretrained teacher network. As suggested in [12], [34], we design a student network structured identically to the teacher network. Such an architecture manifests a two-fold essentiality in terms of: (1) the information loss in distillation (e.g., feature compression/transformation) can be mitigated; (2) the intermediate features can be effectively utilized. We next proceed to explain how to fully exploit the rich features to empower the student learning.

B. Optimization

The optimization of the student network is realized based on the trained teacher network via knowledge distillation. In particular, a core issue for an ideal distillation strategy is the selection of layers to distill knowledge. To completely exploit the advantage of the teacher, we draw inspiration from the previous feature-based distillation schemes [33], [28] by accumulating the features with different scales to enrich the representation. Given a point cloud sample \mathbf{M}_m^c with the label of normal category, we define the output of the teacher network at the position i as $\mathbf{F}_i^T(\mathbf{M}_m^c)$. Analogous to that of the teacher, the feature regressed by the student network is represented as $\mathbf{F}_i^S(\mathbf{M}_m^c)$. Both $\mathbf{F}_i^T(\mathbf{M}_m^c)$ and $\mathbf{F}_i^S(\mathbf{M}_m^c)$ are given by vectors with the dimensions of h_i . In our implementation, we employ a triplet of distillation positions (i.e., $i \in \{1, 2, 3\}$) by setting $(h_1, h_2, h_3) = (128, 512, 2048)$. Note that the features given by both the teacher and student are processed with the max-pooling operation right before the final output. Hence, each output vector can represent more global features with the corresponding scale to better fulfill AD for objects' structure.

Previous works [4], [11] generally adopt $L2$ (or $L1$) loss between the student and teacher output for student training. In the case of our framework, however, we have noticed that such an optimization strategy is prone to poor performance. The reason is that, different from images that are naturally ordered, there is no innate ordering between 3D points, and adopting the $L2$ distance will break the required permutation invariance and manually impose dependencies in the optimization.

To achieve a scale-invariant and order-invariant training strategy, we adopt the cosine-similarity metric between each extracted teacher-student feature pair. For the i -th pair, we encourage the angle of the student's output to approximate the

corresponding teacher's output by *minimizing* the following objective:

$$\mathcal{L}_i(\mathbf{M}_m^c) = 1 - \frac{\mathbf{F}_i^S(\mathbf{M}_m^c) \cdot \mathbf{F}_i^T(\mathbf{M}_m^c)}{\max(\|\mathbf{F}_i^S(\mathbf{M}_m^c)\|_2 \times \|\mathbf{F}_i^T(\mathbf{M}_m^c)\|_2, \epsilon)}, \quad (1)$$

where ϵ is a constant introduced to ensure numerical stability. The other constant 1 is added to fit the objective value into $[0, 2]$ to ease subsequent evaluation without hindering the network optimization. We then average Eq. 1 at all the positions with respect to the whole training set \mathcal{M}^c to form the final training loss for our student network:

$$\mathcal{L} = \sum_{m=1}^{N_c} \frac{1}{3} \sum_{i=1}^3 \mathcal{L}_i(\mathbf{M}_m^c), i \in \{1, 2, 3\}. \quad (2)$$

The pretrained teacher network is kept frozen while optimizing the student network to circumvent the issue of trivial parameterization [10]. Eventually, *minimizing* Eq. 2 motivates the student to mimic the teacher's behavior in terms of a coarse to fine level of learned representations. Our method requires a category-specific student retraining to allow for detecting anomalous point cloud when the definition of the normal label changes.

Importantly, our framework enjoys an essential advantage that the knowledge transferred by the teacher greatly alleviates the sample reliance in training the student network. More precisely, we only use one to five normal samples for the student training to achieve an improved detection performance compared with prior work [23] that involves a large number of training samples to learn features for reconstruction. Such a property also yields a significantly low computational complexity for the student retraining compared with [23].

C. Inference

The trained teacher-student network pair can be jointly leveraged to detect anomalous point cloud. For a test sample $\mathbf{T}^{c_u} \in \mathbb{R}^{w \times 3}$ including w points, our target is to determine whether the unknown label c_u belongs to the normal category c_n . Since the student network is trained only to represent the point cloud labeled by c_n , the anomalous sample should incur a significantly differed teacher-student feature pair. We thus directly forward \mathbf{T}^{c_u} to the teacher and student paths to respectively calculate the feature vectors. Based on the features, we calculate the anomaly score via Eq. 1. We can then evaluate the degree of anomaly by comparing the computed anomaly score with a predefined threshold. Note that we only use the anomaly score at the final position (i.e., $i = 3$) during the test stage. Please refer to Sec. IV-D for a detailed ablation study.

IV. EXPERIMENT

A. Dataset and Implementation Details

Following the previous point cloud-related literature [17], [35], we evaluate our method on the large-scale 3D point cloud dataset: ShapeNet part dataset [38]. It provides per-point annotation for 16 separate shape categories of objects (airplane, bag, cap, etc). We use the official train/test split with 12,137 samples for training and 2,874 samples for test. Each training

and test sample consists of 2,048 randomly sampled points (i.e., $W = 2048$). For the teacher network, we pretrain it for 251 epochs on all the 16 categories in the ShapeNet-Part dataset, following [37]. For the student network, we train it only on a selected normal category with very few samples (1 to 5) for 20 epochs. Both the teacher and student networks are optimized with the ADAM optimizer based on an exponentially decaying learning with the initial value of $1e-3$.

B. Evaluation Metric

We use the area under the Receiver Operating Characteristic (ROC) curve to quantitatively assess our method. The ROC curve reflects the relationship between the True-Positive Rate (TPR, $\overline{TP}/(\overline{TP} + \overline{FN})$) and False Positive Rate (FPR, $\overline{FP}/(\overline{FP} + \overline{TN})$) under varying thresholds, where \overline{TP} , \overline{FN} , \overline{FP} , \overline{TN} denote the number of true positive, false negative, false positive, and true negative samples, respectively. The Area Under the Curve (AUC) metric then computes the whole area under such an ROC curve, and a larger AUC indicates a higher detection capability.

C. Comparative Results

Quantitative Results. We first report the quantitative results in terms of detection accuracy. We compare our method against the closest state of the art [23] that handles the same problem as ours. We give a comprehensive evaluation of detection performance, in which the student network is retrained on each category for different normal category assumptions (i.e., when a certain category is treated as normal, the remaining 15 categories are treated as anomalous). To manifest the ability of our method in handling few samples, during the training for each category selected as normal, we randomly sample 1, 3, or 5 point clouds from the corresponding category, and then train [23] on the same sampled data as ours to make the training protocol for both methods consistent. *Note that the comparison is, however, not fair because (i) the [23] is not originally designed for dealing with few samples as ours; (ii) our framework involves a teacher pretraining stage, whereas [23] does not. Therefore, the comparative results are only focused on presenting the efficiency of our teacher-student framework in modeling the required normal categories with few samples.*

The results are summarized in Tab. I. It can be clearly observed that the proposed method outperforms [23] in detection accuracy by a large margin for almost all categories and sample number settings. This is because the limited training samples considerably degenerate the reconstruction strength of the VAE model in [23], causing the chamfer distance between normal and anomalous categories to be less sensitive to fulfill the detection. The fact that the AUCs for each category of [23] grow positively related to the training sample number further evidences this.

In general, unlike [23], our method does not show noticeable reliance on the training sample number. More precisely, for some categories, even one training sample yields the highest AUCs (5th column in Tab. I). We expect this to be attributed to the fact that the pretrained teacher network well compensates

for the lack of samples for student training, which also justifies the large AUC gap between ours and [23].

Qualitative Results. We next qualitatively investigate our method to provide more insights. Fig. 3 visualizes several detection results for some categories on both normal and anomalous test samples. It can be seen in Fig. 3 that the shape diversity within each category has a huge impact on the detection accuracy. The more diversified the object shapes are, the more challenging the detection will be. For example, both our method and [23] perform well on the category of “Airplane”, where almost all the training/test samples are similar (Fig. 3(a)). However, in the case of “Lamp” (Fig. 3(c)), because the training and test samples have remarkably separate shapes (e.g., width or straightness of the lamp body), both methods tend to fail, which is also reflected in the low AUC in Tab. I (10th row).

Furthermore, reconstruction-based method can neglect some fine object features and only concentrates on the global shape. For example, when dealing with the category “Mug”, the method by [23] cannot well capture the thin line above the lamp (last column in Fig. 3(b)), wrongly classifying the lamp sample as normal. Contrarily, our method handles such a case successfully because we employ the multi-scale training loss to extract features at different levels.

D. Ablation Studies

To provide a deeper understanding of our model, we here analyze the effects of our model regarding the following aspects:

Data Sampling for Training. Our proposed model requires only one to five randomly chosen normal samples for training, which can impose the training stochasticity that stems from the quality of the sampled point clouds. To analyze the underlying effect, we conduct 10 runs in Tab. I by sampling different point clouds. For fair comparisons, all the experimental settings for training and testing [23] are kept the same. As indicated by the average standard deviation in Tab. I (last row), our method is less dependent than [23] on sample number (i.e., the value is much smaller), especially regarding the cases of more than one sample. In particular, using three or five results shows stable performance. We thus set the sample number to five for all the following ablations since it performs the best.

Scales of Features for Test. Although we employ multi-scale training loss to facilitate the feature matching at different positions, the issue of which feature contributes the most to the test performance remains unexplored. We thus evaluate the detection performance by using multi-scale and single-scale anomaly scores for inference to respectively examine the contribution of different positions. We follow Eq. 2 to calculate the multi-scale anomaly score. For the single-scale case, we compute the anomaly score at the final scale ($i = 3$) via Eq. 1. We can observe in Fig. 4 that single- and multi-scale cases generally perform comparably, with the single-scale anomaly score performing marginally better. Motivated by this observation, we simply follow the single-scale test policy in all the experiments.

Different Types of Anomaly Scores for Test To show how the different anomaly scores affect the performance, we compare

TABLE I: The first column depicts the target category for training (i.e., the normal category). When a target category is determined, the other 15 categories are treated as anomalous categories. Each row denotes the quantitative comparison with respect to category-wise AUC (%) metric against [23] on each category with a different number of training samples (i.e., 1, 3, 5). For example, when “Airplane” is the target category, 341 normal airplane tests and another 2,533 anomalous tests are used for testing. The digits to the left and right of “ \pm ” denote the average AUC and the standard derivation for 10 runs with randomly selected training samples, respectively. The best result of each row is in bold.

Category (#tests)	Reconstruction-based method [23]			Knowledge-distillation-based method (Ours)		
	1 sample	3 samples	5 samples	1 sample	3 sample	5 samples
Airplane (341)	87.60 \pm 5.99	96.07 \pm 1.07	97.39 \pm 0.48	97.41 \pm 1.01	98.59 \pm 0.18	98.29 \pm 0.53
Bag (14)	47.09 \pm 8.73	52.41 \pm 5.86	58.70 \pm 5.79	96.88 \pm 3.73	98.23 \pm 2.13	99.94 \pm 0.08
Cap (11)	38.71 \pm 5.70	45.22 \pm 3.82	46.31 \pm 6.38	90.96 \pm 5.54	94.96 \pm 3.05	94.13 \pm 2.94
Car (158)	62.28 \pm 3.27	64.12 \pm 2.06	65.14 \pm 1.81	99.33 \pm 0.27	99.36 \pm 0.26	99.31 \pm 0.29
Chair (704)	49.20 \pm 4.27	53.38 \pm 2.96	55.38 \pm 1.29	95.16 \pm 2.20	98.54 \pm 0.64	98.72 \pm 0.18
Earphone (14)	38.78 \pm 7.61	45.36 \pm 7.26	43.64 \pm 3.21	81.97 \pm 23.45	91.31 \pm 3.07	90.19 \pm 2.22
Guitar (159)	71.75 \pm 3.45	76.13 \pm 3.74	77.59 \pm 2.57	98.65 \pm 0.54	97.66 \pm 1.13	98.39 \pm 0.69
Knife (80)	66.46 \pm 4.20	70.49 \pm 2.31	71.79 \pm 0.91	95.18 \pm 1.75	95.33 \pm 2.22	96.72 \pm 1.08
Lamp (286)	53.09 \pm 5.02	58.68 \pm 2.55	62.20 \pm 3.68	56.13 \pm 6.16	60.76 \pm 8.34	61.22 \pm 5.84
Laptop (83)	67.36 \pm 4.52	69.08 \pm 2.24	70.24 \pm 2.58	98.89 \pm 0.16	98.78 \pm 0.32	98.69 \pm 0.29
Motorbike (51)	82.55 \pm 2.75	87.66 \pm 1.28	88.09 \pm 2.56	90.63 \pm 26.57	99.27 \pm 0.72	99.35 \pm 0.60
Mug (38)	44.04 \pm 5.67	46.94 \pm 2.44	48.55 \pm 3.82	99.60 \pm 0.49	99.73 \pm 0.37	99.35 \pm 0.57
Pistol (44)	64.85 \pm 4.70	71.77 \pm 4.41	78.57 \pm 4.44	99.08 \pm 0.66	98.86 \pm 0.51	98.80 \pm 0.48
Rocket (12)	55.25 \pm 2.97	55.95 \pm 5.69	59.67 \pm 5.05	96.63 \pm 1.44	95.73 \pm 2.01	96.23 \pm 2.93
Skateboard (31)	47.84 \pm 5.19	57.56 \pm 5.08	57.29 \pm 6.62	96.16 \pm 1.20	95.64 \pm 1.06	96.07 \pm 1.11
Table (848)	47.39 \pm 14.48	61.97 \pm 14.66	78.78 \pm 4.56	83.46 \pm 8.17	89.77 \pm 2.34	90.40 \pm 1.05
Avg. AUC	57.77	63.30	66.21	92.26	94.53	94.74
Avg. of Std. Dev.	5.53	4.21	3.48	5.21	1.77	1.30






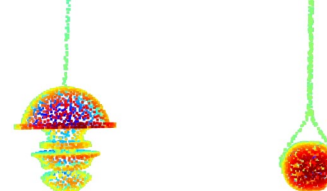
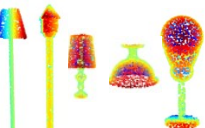
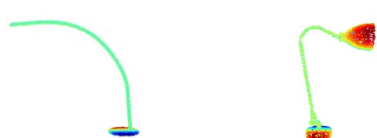

(a)	Airplane	Airplane	Table
		 Ours : \checkmark Masuda et al. : \checkmark	 Ours : \checkmark Masuda et al. : \checkmark
(b)	Mug	Mug	Lamp
		 Ours : \checkmark Masuda et al. : \checkmark	 Ours : \checkmark Masuda et al. : \times
(c)	Lamp	Lamp	Knife
		 Ours : \times Masuda et al. : \times	 Ours : \times Masuda et al. : \times
	Training samples	Normal samples (Test)	Anomalous samples (Test)

Fig. 3: Qualitative comparisons of three selected categories for normal and anomalous samples. The columns from left to right denote training samples, normal test samples, and anomalous test samples, respectively. The training/test category for the cell is explained in the upper-right corner. (a) \sim (c) show three detection results for each assumed normal category in the left-most cell. We use “ \checkmark ” and “ \times ” to respectively indicate the detection success or failure.

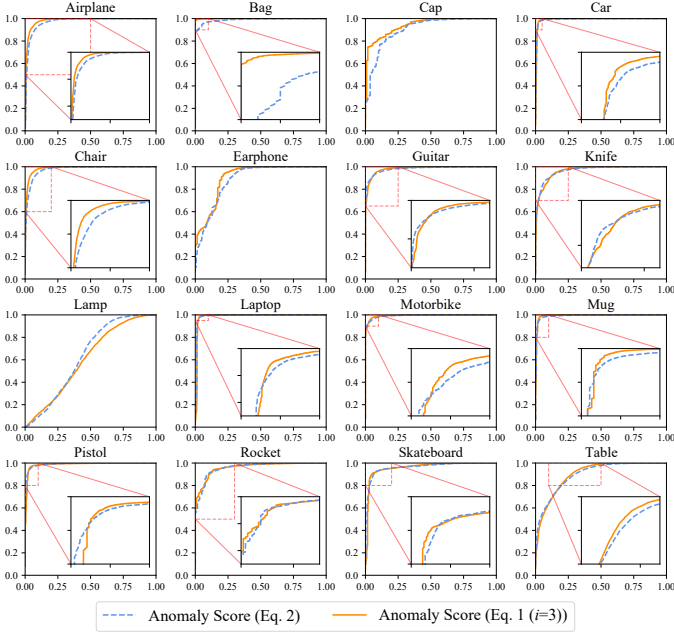


Fig. 4: ROC curve of Anomaly Score at different designed scales. Test performance in each category was evaluated by the final scale and multi-scale anomaly score separately.

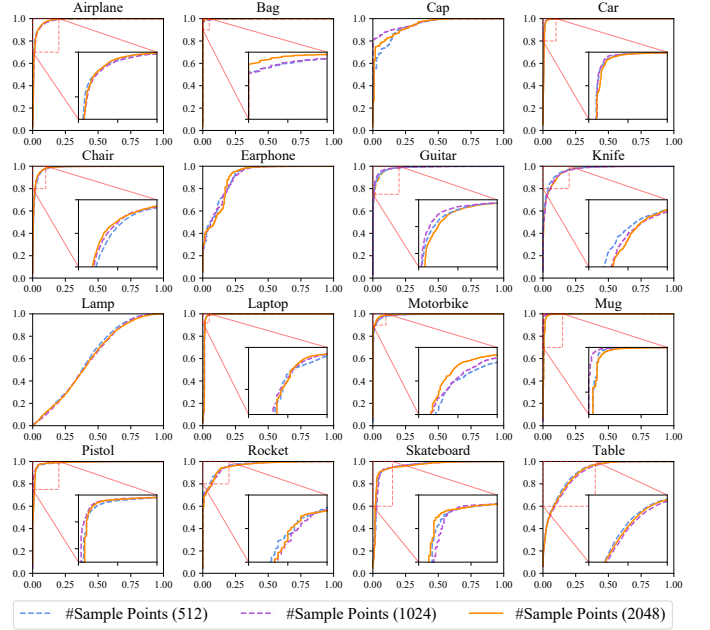


Fig. 6: Comparison of results at different sample points. Test performance in each category was evaluated by using 512, 1,024, and 2,048 sample points separately.

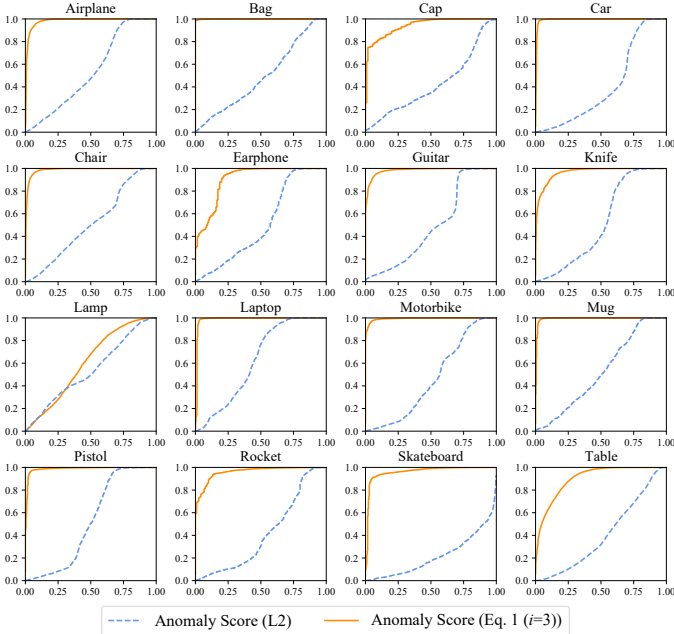


Fig. 5: ROC curve of Anomaly Score at different designed losses. Test performance in each category was evaluated by using the L_2 and cosine similarity anomaly score separately.

the designed anomaly score (i.e., cosine similarity) against the L_2 metric during inference. As shown in Fig. 5, the cosine similarity-based anomaly score significantly outperforms the L_2 metric for almost all categories, demonstrating its capacity in capturing scale-invariant features for detection.

Number of Points. We train and test our model using different numbers of sample points for the point cloud to investigate the impact. We can observe in Fig. 6 that more sampled points

yield a stronger representation for object shape, thus leading to higher detection performance in many cases. However, the change of detection accuracy does not vary greatly.

V. CONCLUSION

In this paper, we have proposed a novel teacher-student network for 3D point cloud anomaly detection with only few normal samples. We also introduce a multi-scale loss function to exploit the potentially beneficial features during training. Extensive experimental results on a large-scale point cloud dataset demonstrate that our method outperforms the state of the art with respect to detection accuracy and dependence on the number of samples. The ablation study further justifies our method.

Our method involves a major limitation if the selected normal category includes highly diversified object shapes. This is mainly because the randomly sampled few training data generally do not cover the diverse shape modes in each category. In the future, we would like to introduce a sampling strategy to explicitly encourage a rich shape coverage within the few training samples.

VI. ACKNOWLEDGEMENT

This work is supported by JSPS KAKENHI Grant Number JP20K19568. We also acknowledge China Scholarship Council (CSC) for funding the first author under Grant Number 202108330097.

REFERENCES

- [1] S. Adhikary and A. Ghosh. Dynamic time warping approach for optimized locomotor impairment detection using biomedical signal processing. *Biomedical Signal Processing and Control*, 72:103321, 2022.

- [2] S. Akcay, A. Atapour-Abarghouei, and T. P. Breckon. Ganomaly: Semi-supervised anomaly detection via adversarial training. In *Asian conference on computer vision*, pages 622–637. Springer, 2018.
- [3] N. Bendre, H. T. Marín, and P. Najafirad. Learning from few samples: A survey. *arXiv preprint arXiv:2007.15484*, 2020.
- [4] P. Bergmann, M. Fauser, D. Sattlegger, and C. Steger. Uninformed students: Student-teacher anomaly detection with discriminative latent embeddings. In *Proceedings of the IEEE/CVF Conference on Computer Vision and Pattern Recognition*, pages 4183–4192, 2020.
- [5] P. Bergmann, X. Jin, D. Sattlegger, and C. Steger. The mvtec 3d-ad dataset for unsupervised 3d anomaly detection and localization. *arXiv preprint arXiv:2112.09045*, 2021.
- [6] P. Bergmann and D. Sattlegger. Anomaly detection in 3d point clouds using deep geometric descriptors. *arXiv preprint arXiv:2202.11660*, 2022.
- [7] L. Chen, Z. You, N. Zhang, J. Xi, and X. Le. Utrad: Anomaly detection and localization with u-transformer. *Neural Networks*, 147:53–62, 2022.
- [8] J. Collins, S. Goel, K. Deng, A. Luthra, L. Xu, E. Gundogdu, X. Zhang, T. F. Y. Vicente, T. Dideriksen, H. Arora, et al. Abo: Dataset and benchmarks for real-world 3d object understanding. In *Proceedings of the IEEE/CVF Conference on Computer Vision and Pattern Recognition*, pages 21126–21136, 2022.
- [9] R. de Paula Monteiro, M. C. Lozada, D. R. C. Mendieta, R. V. S. Loja, and C. J. A. Bastos Filho. A hybrid prototype selection-based deep learning approach for anomaly detection in industrial machines. *Expert Systems with Applications*, page 117528, 2022.
- [10] H. Deng and X. Li. Anomaly detection via reverse distillation from one-class embedding. In *Proceedings of the IEEE/CVF Conference on Computer Vision and Pattern Recognition*, pages 9737–9746, 2022.
- [11] X. Du, X. Wang, G. Gozum, and Y. Li. Unknown-aware object detection: Learning what you don’t know from videos in the wild. In *Proceedings of the IEEE/CVF Conference on Computer Vision and Pattern Recognition*, pages 13678–13688, 2022.
- [12] J. Gou, B. Yu, S. J. Maybank, and D. Tao. Knowledge distillation: A survey. *International Journal of Computer Vision*, 129(6):1789–1819, 2021.
- [13] S. Jain, G. Seth, A. Paruthi, U. Soni, and G. Kumar. Synthetic data augmentation for surface defect detection and classification using deep learning. *Journal of Intelligent Manufacturing*, pages 1–14, 2020.
- [14] L. Jiang, Y. Wang, Z. Tang, Y. Miao, and S. Chen. Casting defect detection in x-ray images using convolutional neural networks and attention-guided data augmentation. *Measurement*, 170:108736, 2021.
- [15] Y. Khalifa, D. Mandic, and E. Sejdić. A review of hidden markov models and recurrent neural networks for event detection and localization in biomedical signals. *Information Fusion*, 69:52–72, 2021.
- [16] D. Kimura, S. Chaudhury, M. Narita, A. Munawar, and R. Tachibana. Adversarial discriminative attention for robust anomaly detection. In *Proceedings of the IEEE/CVF Winter Conference on Applications of Computer Vision*, pages 2172–2181, 2020.
- [17] R. Klokov and V. Lempitsky. Escape from cells: Deep kd-networks for the recognition of 3d point cloud models. In *Proceedings of the IEEE international conference on computer vision*, pages 863–872, 2017.
- [18] J. U. Ko, K. Na, J.-S. Oh, J. Kim, and B. D. Youn. A new auto-encoder-based dynamic threshold to reduce false alarm rate for anomaly detection of steam turbines. *Expert Systems with Applications*, 189:116094, 2022.
- [19] P. Kumari and M. Saini. An adaptive framework for anomaly detection in time-series audio-visual data. *IEEE Access*, 10:36188–36199, 2022.
- [20] C.-L. Li, K. Sohn, J. Yoon, and T. Pfister. Cutpaste: Self-supervised learning for anomaly detection and localization. In *Proceedings of the IEEE/CVF Conference on Computer Vision and Pattern Recognition*, pages 9664–9674, 2021.
- [21] Y. Liao, J. Xie, and A. Geiger. Kitti-360: A novel dataset and benchmarks for urban scene understanding in 2d and 3d. *IEEE Transactions on Pattern Analysis and Machine Intelligence*, 2022.
- [22] J. Lu, P. Gong, J. Ye, and C. Zhang. Learning from very few samples: A survey. *arXiv preprint arXiv:2009.02653*, 2020.
- [23] M. Masuda, R. Hachiuma, R. Fujii, H. Saito, and Y. Sekikawa. Toward unsupervised 3d point cloud anomaly detection using variational autoencoder. In *2021 IEEE International Conference on Image Processing (ICIP)*, pages 3118–3122. IEEE, 2021.
- [24] G. Pang, C. Ding, C. Shen, and A. v. d. Hengel. Explainable deep few-shot anomaly detection with deviation networks. *arXiv preprint arXiv:2108.00462*, 2021.
- [25] W. H. Pinaya, P.-D. Tudosiu, R. Gray, G. Rees, P. Nachev, S. Ourselin, and M. J. Cardoso. Unsupervised brain imaging 3d anomaly detection and segmentation with transformers. *Medical Image Analysis*, 79:102475, 2022.
- [26] C. R. Qi, H. Su, K. Mo, and L. J. Guibas. Pointnet: Deep learning on point sets for 3d classification and segmentation. In *Proceedings of the IEEE conference on computer vision and pattern recognition*, pages 652–660, 2017.
- [27] K. Roth, L. Pemula, J. Zepeda, B. Schölkopf, T. Brox, and P. Gehler. Towards total recall in industrial anomaly detection. In *Proceedings of the IEEE/CVF Conference on Computer Vision and Pattern Recognition*, pages 14318–14328, 2022.
- [28] M. Salehi, N. Sadjadi, S. Baselizadeh, M. H. Rohban, and H. R. Rabiee. Multiresolution knowledge distillation for anomaly detection. In *Proceedings of the IEEE/CVF conference on computer vision and pattern recognition*, pages 14902–14912, 2021.
- [29] K. Sato, S. Nakata, T. Matsubara, and K. Uehara. Few-shot anomaly detection using deep generative models for grouped data. *IEICE TRANSACTIONS on Information and Systems*, 105(2):436–440, 2022.
- [30] Y. Shen, Z. Zhang, M. R. Sabuncu, and L. Sun. Real-time uncertainty estimation in computer vision via uncertainty-aware distribution distillation. In *Proceedings of the IEEE/CVF Winter Conference on Applications of Computer Vision*, pages 707–716, 2021.
- [31] S. Sheynin, S. Benaim, and L. Wolf. A hierarchical transformation-discriminating generative model for few shot anomaly detection. In *Proceedings of the IEEE/CVF International Conference on Computer Vision*, pages 8495–8504, 2021.
- [32] D.-M. Tsai, S.-K. S. Fan, and Y.-H. Chou. Auto-annotated deep segmentation for surface defect detection. *IEEE Transactions on Instrumentation and Measurement*, 70:1–10, 2021.
- [33] G. Wang, S. Han, E. Ding, and D. Huang. Student-teacher feature pyramid matching for unsupervised anomaly detection. *arXiv preprint arXiv:2103.04257*, 2021.
- [34] L. Wang and K.-J. Yoon. Knowledge distillation and student-teacher learning for visual intelligence: A review and new outlooks. *IEEE Transactions on Pattern Analysis and Machine Intelligence*, 2021.
- [35] Y. Wang, Y. Sun, Z. Liu, S. E. Sarma, M. M. Bronstein, and J. M. Solomon. Dynamic graph cnn for learning on point clouds. *Acm Transactions On Graphics (tog)*, 38(5):1–12, 2019.
- [36] Y. Wang, Q. Yao, J. T. Kwok, and L. M. Ni. Generalizing from a few examples: A survey on few-shot learning. *ACM computing surveys (csur)*, 53(3):1–34, 2020.
- [37] X. Yan. Pointnet/pointnet++ pytorch. https://github.com/yanx27/Pointnet_Pointnet2_pytorch, 2019.
- [38] L. Yi, V. G. Kim, D. Ceylan, I.-C. Shen, M. Yan, H. Su, C. Lu, Q. Huang, A. Sheffer, and L. Guibas. A scalable active framework for region annotation in 3d shape collections. *ACM Transactions on Graphics (ToG)*, 35(6):1–12, 2016.
- [39] L. Yi, L. Shao, M. Savva, H. Huang, Y. Zhou, Q. Wang, B. Graham, M. Engelcke, R. Klokov, V. Lempitsky, et al. Large-scale 3d shape reconstruction and segmentation from shapenet core55. *arXiv preprint arXiv:1710.06104*, 2017.
- [40] J. P. Yun, W. C. Shin, G. Koo, M. S. Kim, C. Lee, and S. J. Lee. Automated defect inspection system for metal surfaces based on deep learning and data augmentation. *Journal of Manufacturing Systems*, 55:317–324, 2020.
- [41] S. Zhang, F. Ye, B. Wang, and T. G. Habetler. Few-shot bearing anomaly detection via model-agnostic meta-learning. In *2020 23rd International Conference on Electrical Machines and Systems (ICEMS)*, pages 1341–1346. IEEE, 2020.
- [42] H. Zhao, Y. Li, N. He, K. Ma, L. Fang, H. Li, and Y. Zheng. Anomaly cyberfor for medical images using self-supervised and translation-consistent features. *IEEE Transactions on Medical Imaging*, 40(12):3641–3651, 2021.
- [43] X. Zheng, H. Wang, J. Chen, Y. Kong, and S. Zheng. A generic semi-supervised deep learning-based approach for automated surface inspection. *IEEE Access*, 8:114088–114099, 2020.
- [44] X. Zhou, W. Liang, S. Shimizu, J. Ma, and Q. Jin. Siamese neural network based few-shot learning for anomaly detection in industrial cyber-physical systems. *IEEE Transactions on Industrial Informatics*, 17(8):5790–5798, 2020.
- [45] J.-Y. Zhu, T. Park, P. Isola, and A. A. Efros. Unpaired image-to-image translation using cycle-consistent adversarial networks. In *Proceedings of the IEEE international conference on computer vision*, pages 2223–2232, 2017.